Research Article
doi.org/10.1002/cplu.202400521

Chemistry Europe
European Chemical Societies Publishing

www.chempluschem.org

Platelet Ceria Catalysts from Solution Combustion and Effect of Iron Doping for Synthesis of Dimethyl Carbonate from CO_2

Nicoletta Rusta,[a, b] Valentina Mameli,*[a, b] Pier Carlo Ricci,[c] Stefania Porcu,[b, c] Panpailin Seeharaj,[d] Aryane A. Marciniak,[e] Evelyn C. S. Santos,[f] Odivaldo Cambraia Alves,[g] Claudio J. A. Mota,[e, f, h] Elisabetta Rombi,[a, b] and Carla Cannas*[a, b]

Solution combustion (SC) remains among the most promising synthetic strategies for the production of crystalline nanopowders from an aqueous medium, due to its easiness, time and cost-effectiveness, scalability and eco-friendliness. In this work, this method was selected to obtain anisometric ceria-based nanoparticles applied as catalysts for the direct synthesis of dimethyl carbonate. The catalytic performances were studied for the ceria and Fe-doped ceria from SC (CeO_2-SC, $Ce_{0.9}Fe_{0.1}O_2$-SC) in comparison with the ceria nanorods (CeO_2-HT, $Ce_{0.9}Fe_{0.1}O_2$-HT) obtained by hydrothermal (HT) method, one of the most studied systems in the literature. Indeed, the ceria nanoparticles obtained by SC were found to be highly crystalline, platelet-shaped, arranged in a mosaic-like assembly and with smaller crystallite size ($\approx$6 nm *vs.* $\approx$17 nm) and higher surface area (80 $m^2 g^{-1}$ *vs.* 26 $m^2 g^{-1}$) for the undoped sample with respect to the Fe-doped counterpart. Although all samples exhibit an anisometric morphology that should favor the exposition of specific crystalline planes, HT-samples showed better performances due to higher oxygen vacancies concentration and lower amount of strong basic and acid sites.

Introduction

Currently, air pollution and the resulting climate change due to the continuous increase of CO_2 levels in the atmosphere is the most significant environmental problem. Carbon Capture and Utilization technologies (CCU) are one of the approaches to alleviate this problem.[1–4] In particular, the chemical conversion of CO_2 is based on its use as a raw material in many chemical syntheses to form other added value compounds such as methanol,[5,6] formic acid,[7] methane,[8] dimethyl ether[9,10] and dimethyl carbonate.[11,12] Dimethyl carbonate (DMC) is a valuable eco-friendly compound characterized by low toxicity and good biodegradability[13] and is considered one of the most important organic carbonates due to its many applications in various industrial sectors. In fact, it is widely used in the chemistry of dyes, drugs, food and polycarbonate production.[14–16] It is also used as an additive in Pb-free fuel and electrolytes in Li-ion batteries.[17–19]

There are many routes, called traditional routes, to synthesize DMC: the phosgene method, the oxidative carbonylation of methanol, the transesterification method, the alcoholysis of urea. All suffer from serious safety constraints, because of the involvement of toxic chemical substances, both as reagents, catalysts and by-products.[15,20,21] In recent decades, the research has been focused on developing more sustainable synthetic approaches to replace the traditional routes. Currently the attention has been paid on the direct synthesis of DMC from methanol and CO_2, which appears advantageous for different reasons[22]: it converts a waste (*i.e.*, CO_2) into a valuable fuel (*i.e.*, DMC); it is a single reaction step; it requires relatively low cost of operations and low energy; the only by-product is water.[23] However, this synthetic method still remains at laboratory stage because of poor conversions and low DMC yields, on account of the thermodynamic stability and kinetic inertness of CO_2. In order to overcome these drawbacks, it is necessary to design and develop efficient catalysts to active CO_2 at temperatures below 200 °C and simultaneously prevent the breaking of both

[a] N. Rusta, V. Mameli, E. Rombi, C. Cannas
Department of Chemical and Geological Sciences, University of Cagliari, Cagliari, Italy
E-mail: ccannas@unica.it
valentina.mameli@unica.it

[b] N. Rusta, V. Mameli, S. Porcu, E. Rombi, C. Cannas
National Interuniversity Consortium of Materials Science and Technology (INSTM), Florence, Italy

[c] P. C. Ricci, S. Porcu
Department of Physics, University of Cagliari, Cagliari, Italy

[d] P. Seeharaj
Department of Chemistry, King Mongkut's Institute of Technology Ladkraban, Bangkok, Thailand

[e] A. A. Marciniak, C. J. A. Mota
Escola de Química, Universidade Federal do Rio de Janeiro, Rio de Janeiro, Brasil

[f] E. C. S. Santos, C. J. A. Mota
Instituto de Química, Universidade Federal do Rio de Janeiro, Rio de Janeiro, Brazil

[g] O. C. Alves
Instituto de Química, Universidade Federal Fluminense, Niterói, Brazil

[h] C. J. A. Mota
INCT Energia & Ambiente, UFRJ, Brazil

Supporting information for this article is available on the WWW under https://doi.org/10.1002/cplu.202400521

C–O bonds.[24] Nowadays, the most proposed catalysts are ionic liquids,[25] alkali carbonates,[26] metal oxides,[27] and supported catalysts of alloys[28] and metal oxides.[29] Among these reported catalytic systems, ceria-based catalysts are particularly promising due to their chemical stability, easy regenerability, and storage under ambient air. Furthermore, its catalytic property is due to the redox activity of Ce^{4+}/Ce^{3+} species which involves the formation and exposure of active surface cationic sites and oxygen vacancies, O_v, where the latter favor the adsorption and activation of CO_2 molecules.[30,31] Despite these properties, ceria-based catalysts produce relatively low DMC yields, therefore attention is paid on the key parameters that allow improving the catalytic performance of these systems. One of them is the morphology of the catalysts which in fact has a high influence on the exposure of the most active crystalline planes for this specific application and the consequent surface concentration of oxygen vacancies.[32–34] In fact, some of the previous studies on the comparison of the catalytic performances of CeO_2 with different morphologies (rods, spindles, cubes and octahedrons) highlighted that the best catalytic performances are obtained for elongated morphologies such as nanorods and nanospindles, in which a greater exposure of the defective crystalline planes (111) was observed.[35] Nevertheless, a study of nanostructured CeO_2 showed better correlation of the catalytic activity with the (110) exposed plane, which were confirmed by DFT periodical calculations that indicated the easier formation of oxygen vacancy on this plane, as well as the formation of an adsorbed carbonate intermediate upon interaction with the CO_2 molecule.[34] A further key parameter to improve the catalytic performance is CeO_2 doping with other metals, such as Zr,[36] Ti,[37] Zn[38] and Fe.[39] In fact, the incorporation of doping metal promotes the reduction of Ce^{4+} to Ce^{3+} which induces the formation of surface defects, which are active sites for the adsorption and dissociation of CO_2 and methanol to form the intermediate species in the DMC synthesis: methoxy (CH_3O^-) and methoxycarbonyl ($CH_3OCO_2^-$) anions.[40,41] Furthermore, CeO_2 doping could lead to the variation of acid-base sites. More specifically, previous studies highlighted that the doping of ceria with iron improves the catalytic performance as the Fe insertion can influence the amount of surface acid and base sites. Some authors[39] reported for CeO_2 nanorods with Fe doping, a significant increase of the total and the weak + medium acid and basic sites. Some other[42] for CeO_2 nanospindles observed an increase of the total basic sites and the decrease of acid sites after Fe doping. In a previous work,[43] we proposed mixed CeO_2/Fe_2O_3 catalysts and the improved performances were interpreted in terms of the high surface area and high concentration of surface oxygen vacancies together with the exposition of (110) plane on the CeO_2 surface, which is known to favor the formation of oxygen vacancies.

In order to obtain ceria catalysts with the best catalytic performance for the direct synthesis of DMC, numerous synthetic methodologies have been used in the recent years (for a comparison of the pros and cons of the different methods see Table S1).[44–51] However, most of these synthetic strategies require many process steps and long times (2–4 days) to obtain the catalyst, and some may not receive much commercial attention in terms of costs due to the expensive precursors, and surfactants. Instead, solution combustion synthesis (SC) is a simple, one-step, instantaneous and energy-saving synthetic method that allows the obtaining of nanostructured materials with high surface areas.[52] SC synthesis is a self-sustaining thermal process, where the combustion reaction between metal oxidizer and fuel (reducing agent) is the main heat source.[53] The combustion reaction is complete in few minutes at high temperatures and this allows the obtaining of metal oxide nanopowders quickly. In fact, no post-synthesis purification processes are necessary. Furthermore, it is possible to modulate the structural and textural properties of the products by controlling the synthetic parameters that influence the combustion process such as the type of metal oxidizer, fuel type and fuel-to-oxidizer ratio.[54] CeO_2 nanoparticles synthesized via solution combustion synthesis, using different fuels (glycine, urea, hydrazine, glucose, EDTA and citric acid), have been used for different applications, such as photocatalysis,[55,56] water treatment,[57] antibacterial activity studies.[56] On the contrary, CeO_2 synthesized via SC has never been proposed for the direct synthesis of DMC from methanol and CO_2, to the best of our knowledge.

Based on the many advantages on the SC method with respect to those usually applied for the synthesis of CeO_2 -based catalysts, the objective of this contribution is to prepare CeO_2-based nanopowders *via* SC synthesis, due to the possibility of obtaining anisometric platelet shaped nanoparticles and to test them for the direct synthesis of DMC from CO_2. In fact, anisometric-shaped nanoparticles can increase the exposure of defective crystalline planes (111 and 110). The effect of the reducing agent (glycine and citric acid) in modulating the structural and textural properties of the obtained systems was also investigated. Subsequently, the iron doping in the SC synthesis was studied and the two SC systems were compared with the corresponding reference catalysts with rod shape and synthesized via hydrothermal treatment (HT samples). Indeed, as previously mentioned, nanorods represent the system with some of the greatest catalytic activity and for this reason it has been the most investigated for the direct synthesis of DMC. For all systems the catalytic activity was studied at different catalytic conditions and correlated with the microstructural, morphological, textural, basic properties and oxygen vacancies concentration.

Experimental Section

Materials

Cerium(III) nitrate hexahydrate (99.5%, Acros organics) and Iron (III) nitrate nonahydrate (98%, Sigma Aldrich) were used in both synthetic strategies. NaOH (pellets, Sigma Aldrich) and ethanol (96% (v/v), AnalaR NORMAPUR®) were used in hydrothermal synthesis. Citric acid (99.5%, Aldrich) and glycine (99%, Sigma Aldrich) was used in solution-combustion synthesis. Micrometric hematite (99.9%, Aldrich) was used as a reference in Raman measurements ($\lambda_{exc} = 785$ nm). All reagents were used as received without further purification.

Synthesis of Catalysts

Nanostructured catalysts of pure and iron-doped ceria were prepared through two different synthetic strategies. The first, through a solution-combustion synthesis (SC) and the second through a hydrothermal method (HT). In both syntheses the iron-doped catalyst was prepared with a ratio of 0.1 mol of metal dopant ($Ce_{0.9}M_{0.1}O_2$).

Solution-Combustion Synthesis (SC)

10 mL of Cerium(III) nitrate hexahydrate ($Ce(NO_3)_3 \bullet 6H_2O$) aqueous solution (1 M) and 10 mL of citric acid or glycine aqueous solution (1 M) were mixed under vigorous stirring (700 rpm) and left to evaporate at 80 °C until the formation of a colorless viscous liquid with characteristics between a liquid and a gel. Then, the viscous liquid was put for 15 min in a preheated muffle furnace at the temperature of 300 °C to obtain a nanocrystalline CeO_2 powder[58] (Figure 1a). The same procedure was used in the case of the iron-doped sample, in which a Cerium(III) nitrate hexahydrate ($Ce(NO_3)_3 \bullet 6H_2O$) aqueous (0.9 M) and an Iron (III) nitrate nonahydrate ($Fe(NO_3)_3 \bullet 9H_2O$) aqueous solution (0.1 M) were prepared. The obtained samples were denoted CeO_2-SC and $Ce_{0.9}Fe_{0.1}O_2$-SC.

Hydrothermal Synthesis (HT)

The synthesis was conducted by following the procedure reported hereafter.[36] 3.26 g of Cerium(III) nitrate hexahydrate ($Ce(NO_3)_3 \bullet 6H_2O$) was dissolved in 18.75 mL of double-distilled water under vigorous stirring until completely dissolved. At the same time, 53.0 g of sodium hydroxide (NaOH) was dissolved in 131.25 mL of double-distilled water. Next, the two solutions were mixed and kept stirring for 30 min at room temperature. The obtained slurry was transferred into a 210 mL stainless steel autoclave (Berghof DAB-3) and kept at 100 °C for 24 h. After the autoclave was cooled down to room temperature and the products were washed with distilled water until the pH reaches 7 and then washed 3 times with ethanol. The product was dried at 80 °C for 24 h and after calcined at 600 °C for 5 h (with heating rate 5 °C min^{-1}) in a muffle furnace to obtain CeO_2 nanorods catalyst (Figure 1b). Similarly, Fe doped-CeO_2 nanorods catalyst with 0.1 mol ratio of the metal dopant was prepared by adding the corresponding iron precursor to the cerium nitrate solution. The obtained samples were denoted CeO_2-HT and $Ce_{0.9}Fe_{0.1}O_2$-HT.

Characterization of Catalysts

The samples were characterized by powder X-ray diffraction (XRD) in the 2θ range between 15° and 100°using a PANalytical X'pert Pro (Malvern PANalytical, Malvern, UK) with a Cu Kα X-ray source. The refinement of the structural parameters was performed by the Rietveld method using the software MAUD[59] and adopting recommended fitting procedures.[60] The standard reference LaB_6 from NIST was used for determining the instrumental broadening. The CIF structure from Crystallography Open Database (COD) used for the refinement is 1562989 for Ceria and 1011267 from hematite. Raman spectroscopy measurements were conducted using Thermo Scientific, DXR Smart spectrometer with 532 nm solid state laser excitation. In addition, was used a MS750 spectrograph (Sol-Instruments), a 532 nm and 785 nm laser through a 10× Olympus objective lens were used as excitation sources. The analysis of Raman spectra was carried out using Peakfit 4.12 software (Jandel, AISN Software) including background subtraction and curve-fitting procedures. To estimate the average particle size by fitting the

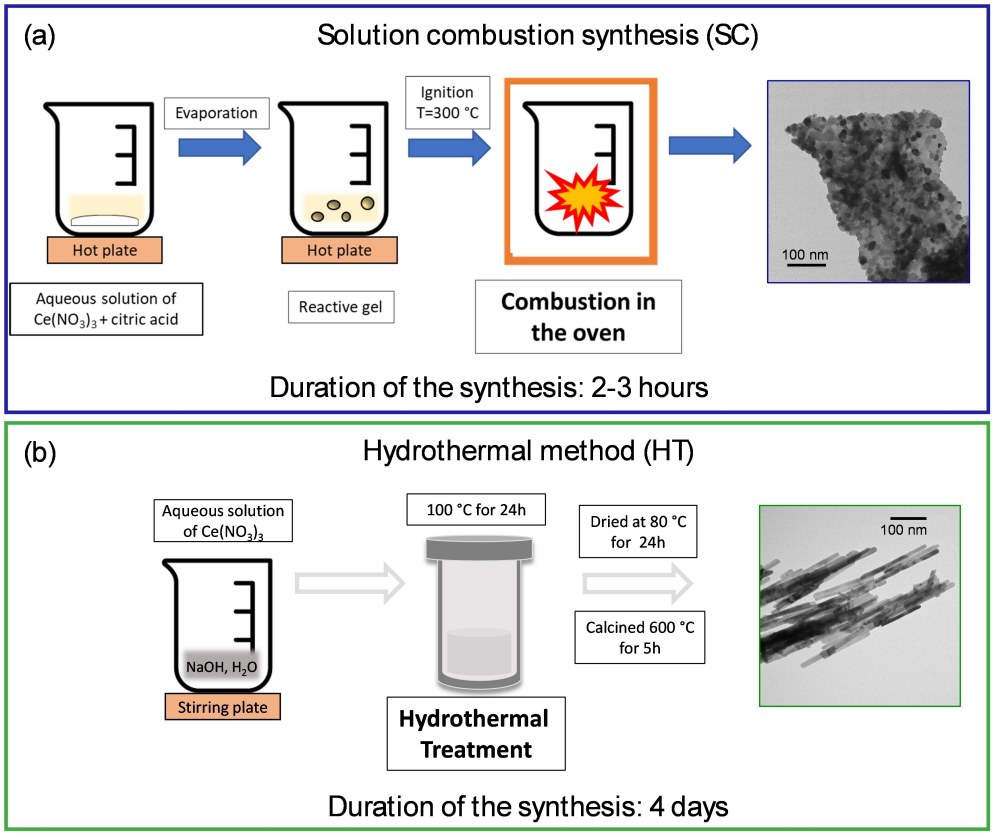

Figure 1. Schematic illustration of the solution combustion synthesis (SC) (a) and hydrothermal method (HT) (b).

Raman spectra, was used the equation FWHM (cm^{-1}) = 10 + 124.7/d_g (nm).[61] A JEOL JEM 1400-PLUS microscope operating at 120 kV were used to obtain the transmission electron microscopy (TEM) micrographs. The analysis of the images for the determination of the particle dimensions was carried out using the "ImageJ" software.[62] Chemical analyses were obtained by STEM-EDX. HRTEM images were acquired on a JEOL 2100F microscope operating at 200 kV. The samples' powders were dispersed in n-octane or ethanol, sonicated, and the resulting suspensions dropped onto 200 mesh carbon-coated copper TEM grids.

The Brunauer-Emmett-Teller (BET) specific surface area was measured by nitrogen adsorption–desorption isotherms at −196 °C, using the Micromeritics ASAP 2020 system. All samples were pre-heated under vacuum at 250 °C (heating rate, 1 °C min^{-1}) for 12 h.

The EPR spectra were recorded on a Bruker EMX Plus spectrometer operating in the X-band (9.7 GHz) at room temperature using 50 mg of sample and a microwave power of 20 mW, amplitude modulation of 5 G, and frequency modulation of 100 kHz. The presence of oxygen vacancies (O_v) in the lattice was evaluated from broad signals in the high-field region with g values of 2.06 and 2.74 to CeO_2-SC and CeO_2-HT, respectively. The spectra were fitted with derivatives of Lorentzian lines with Origin® (Microcal) software. The fitting parameters are the resonant field (HR), the peak-to-peak linewidth (DH) and intensity (y_m). The spectral area was calculated from these three parameters as y_m x $(DH)^2$.

CO_2 and NH_3 temperature-programmed desorption measurements were carried out in a TPD/R/O 1100 apparatus (ThermoQuest) with a thermal conductivity detector (TCD). Before analyses, the samples were pre-treated under N_2 flow (30 mL min^{-1}) at 130 °C for 30 min to remove any surface physiosorbed impurities. After cooling to room temperature, CO_2 flow (20 mL min^{-1}) for 1 h was used to saturate the samples. Then, CO_2 and NH_3 desorption was carried out from 25 °C to 500 °C at a ramping rate of 50 mL min^{-1} under He atmosphere. The quantification of CO_2 and NH_3 TPD profiles was carried out by integrating the area under the curve for the three temperature ranges corresponding to weak, medium and strong basic and acid sites.

Catalytic Activity Test for the Direct Synthesis of DMC from CO_2 and Methanol

The catalytic tests were carried out either in Italy and in Brazil, with slight modification of the experimental procedure.

DMC syntheses were carried out in a 100 mL high-pressure reactor (Berghof or Parr (Figure S1)) under magnetic stirring. About 100 or 200 mg of the synthesized catalyst powders and 15 or 35 mL of methanol (CH_3OH; purity ≥ 99.8 %, Sigma-Aldrich) were charged into the reactor and, before the reaction, the reactor was purged with CO_2 three times to remove air and then pressurized to 3.0 or 5.0 MPa of CO_2 gas (purity 99.9 %). The system was heated to 140 °C (2 or 5 °C min^{-1}) for 2 or 3 h before cooling it down to room temperature and separation of the catalyst powder by centrifugation. The products were analyzed by gas chromatography equipped with a flame ion detector (Agilent Technologies 6890 N GC-FID), using a capillary column (Zebron ZB-WAX, 30 m×0.25 mm×0.25 μm) or gas chromatography-mass spectrometry (Agilent Technologies 7890 A), using a capillary column (J&W HP-5 ms Ultra Inert GC Column, 30 m×0.25 mm×0.25 μm). Helium was used as a carrier gas with a flow rate of 1 mL min^{-1}.

Some reactions were carried out with 300 mg of catalyst, 6 h of reaction time and at 4.0 MPa. In addition, triplicate runs were also carried out in some cases. The DMC yield (mmol g_{cat}^{-1}) was estimated using the following Equation (1).

$$DMC\ yield\ \left(mmol\ g_{cat}^{-1}\right) = \frac{DMC\ formation\ (mmol)}{Catalyst\ (g)} \quad (1)$$

Results and Discussion

A preliminary study for the choice of the more appropriate complexing/reductant agent was conducted by using citric acid and glycine (Figure S2a and b, Figure S3a and b, Table 1) in the solution combustion (SC) synthesis.

Since the surface area (Table 1) is an important feature for catalyst applications, in this work it was decided to focus attention on SC synthesis using citric acid, which allowed obtaining a greater specific surface area, and compare the samples obtained with those prepared with the hydrothermal method. The XRD patterns of CeO_2 and iron doped-CeO_2 catalysts obtained from the solution combustion (SC) and hydrothermal (HT) synthesis are presented in Figure 2. Rietveld refinement was also carried out on the XRD patterns and are shown in Figures S3b, S4 and S5. Both synthetic strategies lead to the obtaining of CeO_2 with different characteristics, shown in Table 2.

The XRD patterns of all catalysts showed the main diffraction peaks CeO_2 with face-centered cubic fluorite structure. The comparison between the CeO_2 samples highlighted a smaller crystallite size (6.26(5) nm *vs.* 21.4(1) nm) and a similar lattice parameter (5.4153(6) Å *vs.* 5.4120(2) Å) for CeO_2-SC with respect to CeO_2-HT, and higher with respect to the theoretical one (5.4113 Å). In the XRD pattern of the $Ce_{0.9}Fe_{0.1}O_2$-SC sample, no peaks related to secondary phases of the dopant were observed (Figure 2 inset). These results confirmed the incorporation of all iron into the lattice of CeO_2, taking into account that no washing steps are carried out during this synthetic procedure. On the contrary, the sample $Ce_{0.9}Fe_{0.1}O_2$-HT showed very weak peaks at 24.1°, 35.6°, 49.5°, 54.0°, 62.5°, and 64.0° 2θ values (Figure 2 inset), corresponding to diffraction phenomena from (012), (110), (024),(116), (214), and (300) planes of hematite (JCPDS card No. 33–0664, space group $R\bar{3}c$), which Rietveld

Table 1. Structural and textural properties of CeO_2 SC sample synthesized by citric acid and glycine as complexing agents.

Sample	Lattice parameter (Å)[a]	Crystallite size $< D_{XRD} >$ (nm)[a]	BET Surface Area (m^2/g)[b]	Average Pore Size (nm)[b]	Pore Volume (cm^3/g)[b]
CeO_2-SC	5.4153(6)	6.26(5)	80	7.8	0.2
CeO_2-GLY	5.4196(3)	12.1(6)	38	0.2	3.5

[a] Rietveld analysis carried out with Maud Software with an isotropic model (Figure S3 a and b). [b] %RSD (S_{BET}) = 2.1 %, %RSD (D_p) = 1.8 %.

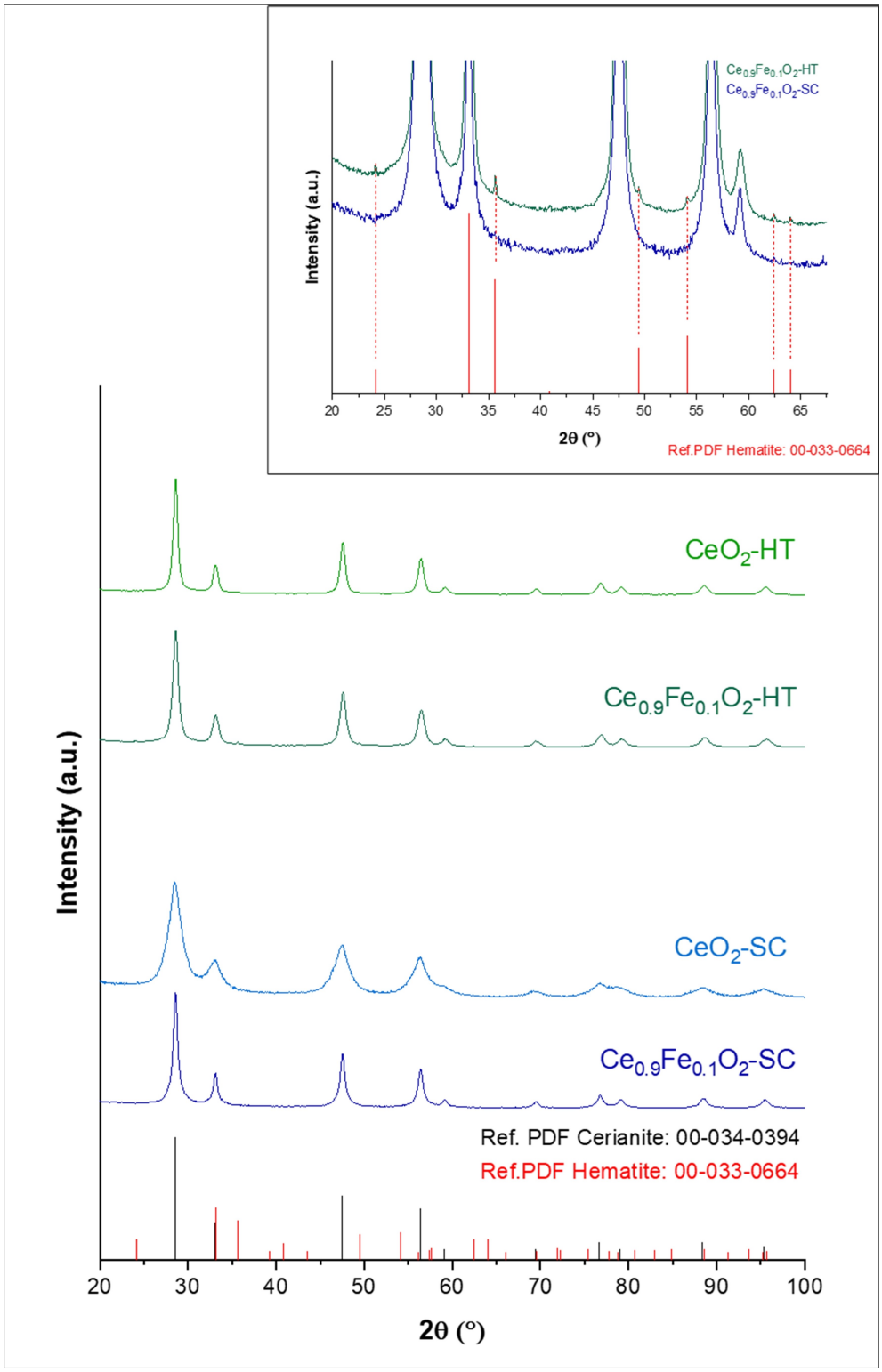

Figure 2. XRD patterns of CeO_2 and Fe-doped CeO_2 synthesized by HT and SC methods. Details on the XRD patterns of the Fe-doped CeO_2 samples (inset).

analysis quantified as approximately 2% (corresponding to a 1.7% of Fe/(Fe+Ce)). This quantity is compatible with the maximum theoretical one of 4.2% of Fe/(Fe+Ce)), calculated from the iron precursor amount used in the synthesis. Based on these data, it is possible to estimate a maximum percentage of about 2.5% of Fe/(Fe+Ce) inside the ceria structure, assuming that all the iron nitrate was involved in the reaction. Nevertheless, it is not possible to exclude that part of the initial iron amount was removed (as iron nitrate or iron oxide) through the washing step. The parameters calculated using the MAUD

Table 2. Structural and textural properties of CeO_2 and Fe-doped CeO_2 synthesized with by HT and SC methods.

Sample	Lattice parameter (Å)[a]	Crystallite size $<D_{XRD}>$ (nm)[a]	Particle size $<D_{Raman}>$ (nm)[b]	C (%)[c]	BET Surface Area (m^2/g)[d]	Average Pore Size (nm)[d]	Pore Volume (cm^3/g)[d]
CeO_2-SC	5.4153(6)	6.26(5)	3.8	3.64(7)	80	7.8	0.2
$Ce_{0.9}Fe_{0.1}O_2$-SC	5.4139(3)	17.10(1)	9.0	0.79(2)	26	1.6	0.1
CeO_2-HT	5.4120(2)	21.4(1)	16.5	0.74(1)	62	2.1	0.4
$Ce_{0.9}Fe_{0.1}O_2$-HT	5.4055(2)	16.14(7)	7.0	-	79	2.6	0.5

[a] Rietveld analysis carried out with Maud Software with an isotropic model. [b] Values obtained considering the F_{2g} vibrational mode of ceria and $\lambda_{exc}=532$ nm. [c] Values obtained by CHN elemental analysis (%RSD (C) = 2%). [d] %RSD (S_{BET}) = 2.1%, %RSD (D_p) = 1.8%.

software showed only a slight decrease in the cell parameter in the doped samples compared to the ceria ones for both syntheses, suggesting no relevant changes in the crystalline lattice. In fact, as reported in Table S1, the ionic radius for Ce^{4+} and Ce^{3+} is in the range 101–128 pm depending on the type of coordination, whereas for Fe^{3+} and Fe^{2+} lower radius are expected (69–92 pm and 75–106 pm, respectively).[63] Therefore, the slight contraction of the lattice is compatible with a partial substitution of Ce species with Fe ones, and it may suggest a 8-fold coordination and a high spin state for the Fe ions, and the reduction of Ce^{4+} to Ce^{3+} to maintain charge neutrality. Indeed, the effect of the reduction in terms of an increase in the ionic radius of Ce is balanced by the substitution of Ce ions by smaller cations.[42] As reported in the literature the reduction led to the formation of oxygen vacancies which have an effect on decreasing the effective anion radius in the ceria lattice, and consequently on the lattice parameter. The Fe-substitution was found to lead to small differences in the lattice parameter in agreement with that found in the literature and slightly higher for the HT samples (0.03% for SC samples, 0.12% for HT samples, 0.05% for [42]).[42] Furthermore, from the crystallite size values obtained, an opposite behavior was observed for the doped samples compared to pure ceria depending on the synthesis method used. An increase was observed for the SC samples (from 6.26(5) nm to 17.10(1) nm). On the contrary, in the case of HT synthesis, the presence of Fe led to a decrease in the crystallite size (from 21.4(1) nm to 16.14(7) nm), in agreement with the literature for Fe-CeO_2 nanorods synthesized by the same hydrothermal method with different Fe content (from 0.5% to 15%) and suggesting the partial insertion of Fe in the ceria lattice. Other authors justified the decrease in the crystallite size as due to the formation of crystalline defects during the hydrothermal reaction.[42] For the SC samples, this unexpected result, in comparison with the HT samples, might be compatible with a different thermal evolution of the solution combustion reaction for the two systems (CeO_2 and $Ce_{0.9}Fe_{0.1}O_2$) causing different crystallite sizes and amounts of carbonaceous residues.

In order to further investigate the microstructural properties of the samples, Raman spectra of CeO_2 and Fe doped-CeO_2 catalysts were collected (Figure 3). Raman spectra collected with $\lambda_{exc}=532$ nm, Figure 3a and b, show a predominant Raman active band centered at about 460 cm^{-1}, ascribed to the F_{2g} mode of the fluorite-like phase. In addition, both HT samples spectra show weak bands at 258 and 595 cm^{-1}, attributed to the second-order transverse acoustic (2TA) mode and defect-induced (D) mode, respectively (Figure 3b).[64,65] The band at 595 cm^{-1} has been primarily attributed to non-stoichiometric longitudinal optical modes related to oxygen vacancies. Oxygen vacancies are a key feature in doped CeO_2 systems, as they are introduced when Ce^{4+} is partially replaced by Fe^{3+}, leading to charge compensation and the creation of vacancies in the oxygen sublattice. In this case, oxygen vacancies are strictly connected to Frenkel defects that occur when oxygen atoms migrate from their normal lattice positions to interstitial sites, leaving behind vacancies. As such, the band at 595 cm^{-1} could arise from the structural disorder associated with both the formation of Frenkel defects and the resulting oxygen vacancies.[66] In contrast, the $Ce_{0.9}Fe_{0.1}O_2$-SC spectrum shows weak bands at approximately 308 cm^{-1} attributed to the second order transverse acoustic mode (2TA) and at around 528 cm^{-1}, another defect-induced mode (D). The band at 528 cm^{-1} is associated with extrinsic oxygen vacancies resulting from the substitution of Ce^{4+} with M^{3+} ions, such as Fe^{3+}. These extrinsic vacancies are distinct from the intrinsic vacancies and Frenkel defects discussed earlier, as they are directly tied to the cation substitution (Figure 3a). The $Ce_{0.9}Fe_{0.1}O_2$-SC sample shows a decrease in the full width at half maximum (FWHM) value of the F_{2g} band with respect to the one of the CeO_2-SC sample, indicative of the increase in particle size, in agreement with the XRD results (crystallite size from ≈6 to ≈17 nm). On the contrary, an increase in the FWHM value of the F_{2g} band is detected for the $Ce_{0.9}Fe_{0.1}O_2$-HT catalyst with respect to the CeO_2-HT sample, suggesting the decrease in the particle size as observed for the crystallite size determined by XRD (from ≈21 to ≈16 nm). The average particle size values estimated by fitting the Raman spectra (Table 2) shows a trend similar to that obtained by XRD.[67,68] No peaks attributable to hematite were observed for both Fe-doped CeO_2 catalysts in the spectra acquired with $\lambda_{exc}=532$ nm. Raman spectra of the Fe-doped CeO_2 catalysts and micrometric hematite (commercial sample) collected using the $\lambda_{exc}=785$ nm laser line are compared in Figure 3c. In agreement with the XRD findings, the $Ce_{0.9}Fe_{0.1}O_2$-SC shows only the CeO_2 band. Whereas additional bands due to hematite (A_{1g} and E_g vibrational modes) are clearly visible for the $Ce_{0.9}Fe_{0.1}O_2$-HT sample, confirming the XRD results.

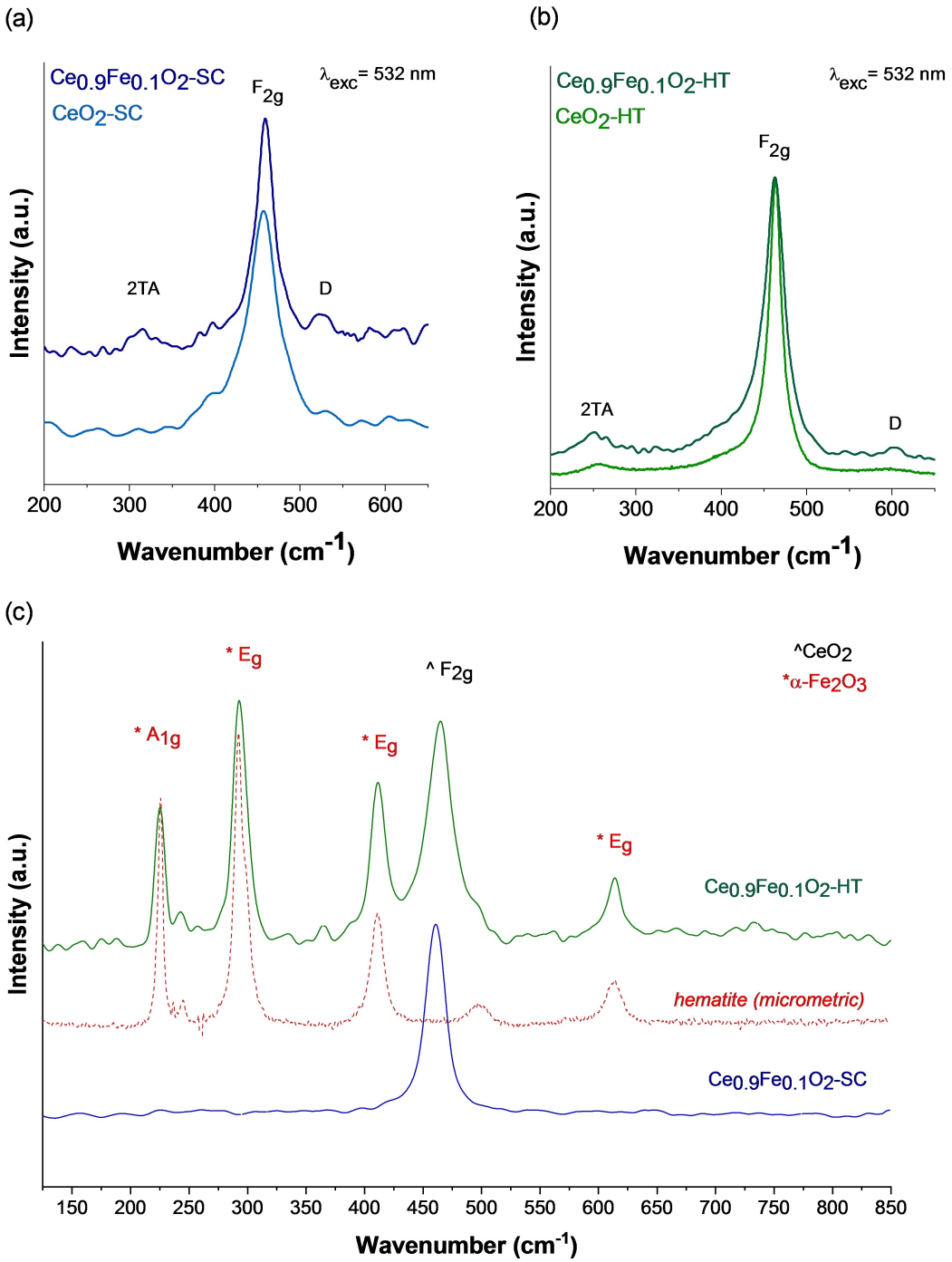

Figure 3. Raman spectra of CeO_2 and Fe-doped CeO_2 synthesized by SC (a) and HT (b) methods using the excitation laser with $\lambda_{exc} = 532$ nm. The inset shows the lower intense defects bands (D). Raman spectra of Fe-doped CeO_2 with $\lambda_{exc} = 785$ nm (c).

The morphology and particle size of the catalysts were studied by conventional TEM and using ImageJ software. The SC samples shown in Figure 4 highlighted the presence of faceted and platelet nanoparticles (red arrows) having various geometries with dimensions ranging from 10 nm to 32 nm for both samples. The lower crystallite size observed by XRD in the CeO_2-SC sample, is compatible with the observation of very thin platelet particles. A very high level of aggregation was observed often forming a mosaic structure, with a higher content of the carbonaceous residues in the ceria sample (in agreement with the elemental analysis reported in Table 2) that makes more difficult the estimation of the particle size. Indeed, the yellow arrows in Figure 4 showed the presence of a carbonaceous matrix with meso- and macroporosity (dimensions between approximately 20 and 110 nm), probably generated through gas evolution during spontaneous combustion. HRTEM micrographs shows the high crystallinity of the faceted nanoparticles both for the ceria sample and for the Fe-doped one. The

Research Article
doi.org/10.1002/cplu.202400521
Chemistry Europe
European Chemical Societies Publishing

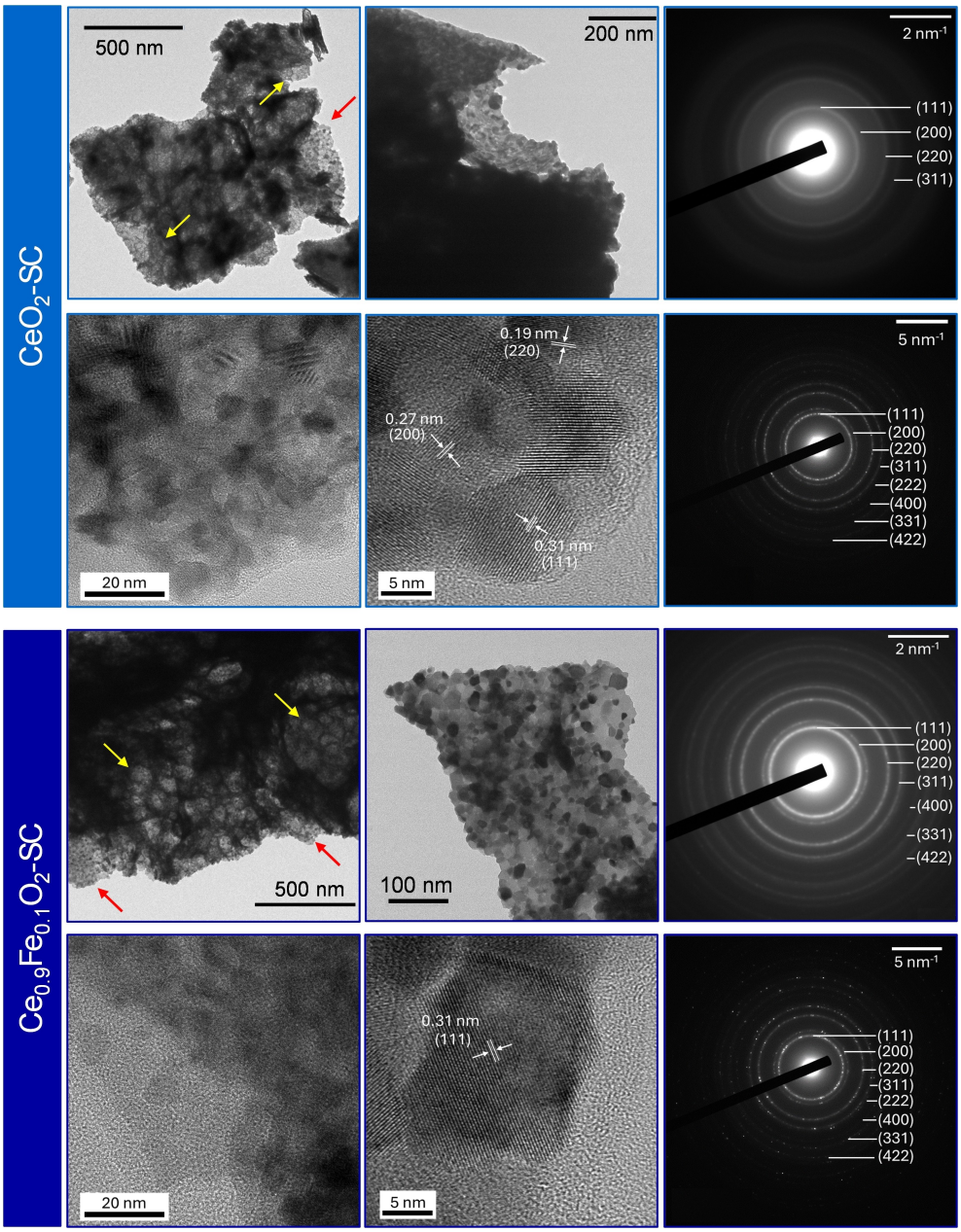

Figure 4. TEM and HRTEM micrographs and selected area electron diffraction of CeO_2 and Fe-doped CeO_2 synthetized by SC method.

observed difference in the particle size estimated by HRTEM for the two samples better agrees with the XRD results, that showed an increase in the crystallite size due to Fe-doping. The estimated interplanar spacings are compatible with (200), (111) and (110) planes of the CeO_2 structure. The SAED analysis confirmed the polycrystalline nature of the platelet nanoparticles, with a better contrast of the diffraction rings in the Fe-doped sample compared to the ceria counterpart, probably due to a lower content of carbonaceous residues. The diffraction rings of the electron diffraction pattern obtained by conventional TEM for the CeO_2-SC are ascribable to the (111), (200), (220), and (311) planes of the cubic CeO_2. In the case of $Ce_{0.9}Fe_{0.1}O_2$-SC, the additional rings associated with (400), (331), and (422) planes of the cubic CeO_2 are also clearly visible.

Figure 5 showed that the particles from the HT samples adopt a nanorod morphology with lengths in the range from 30 to 90 nm and sections from 6.5 to 13 nm, for both samples. The low-magnification micrograph for the $Ce_{0.9}Fe_{0.1}O_2$-HT sample, besides the ceria nanorods, exhibit dark submicrometric regions (yellow arrows), that suggest the presence of a secondary phase. The diffraction rings of the SAED analysis are ascribable to polycrystalline cubic CeO_2 for both samples, but, in the $Ce_{0.9}Fe_{0.1}O_2$-HT sample few additional spots ascribable to hematite monocrystals are also visible, in agreement with XRD and Raman data. The HRTEM highlighted the presence of (111) and (100) planes of the CeO_2 structure.

In order to further investigate the Fe-doped samples, microanalysis from both STEM-EDX from conventional (Fig-

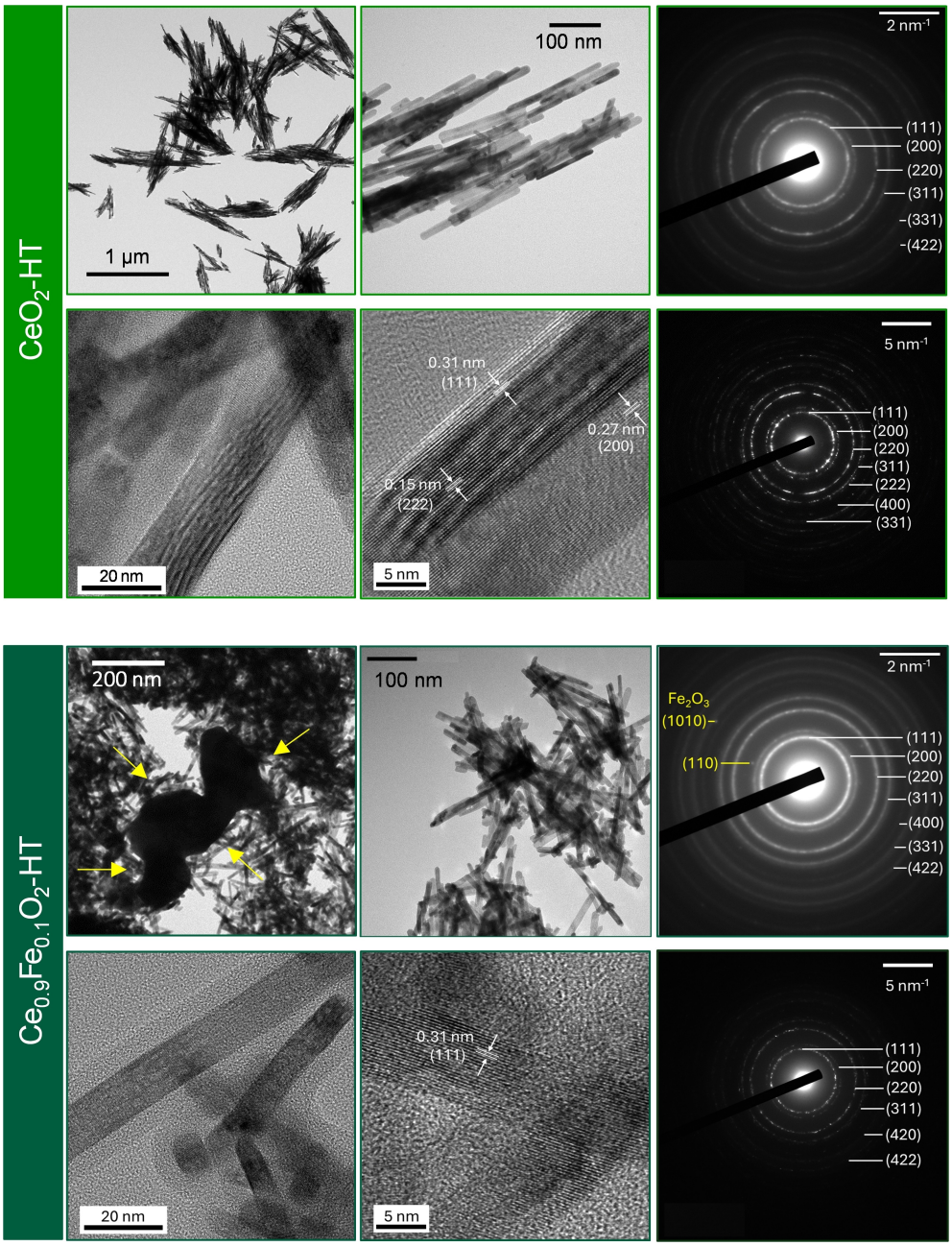

Figure 5. TEM and HRTEM micrographs and selected area electron diffraction of CeO_2 and Fe-doped CeO_2 synthetized by HT method.

ure S7) and HRTEM (Figure 6) were performed. The mean experimental weight percentage Fe/(Fe + Ce) obtained by EDX microanalysis for the SC Fe-doped sample (Figure S8) was found to be about 4.4% in good agreement with the theoretical one of 4.2%. The cerium, oxygen, iron and carbon distribution, both in the elemental chemical mapping and in the normalized linear profiles, are perfectly overlapped in the case of the SC Fe-doped sample, suggesting the incorporation of iron into the cubic CeO_2 structure, as suggested by XRD and Raman data. The same analysis done on the HT Fe-doped sample on three elements (Ce, O, Fe) revealed a homogenous distribution of the three elements by chemical mapping, whereas the linear profile highlighted slight differences in the three profiles, suggesting the copresence of different oxide phases, *i.e.*, Fe-doped ceria together with hematite, in agreement with the XRD, Raman, morphological and diffraction data acquired by conventional TEM. The EDX microanalysis on wide areas (Figure S9) for the HT Fe-doped sample revealed a weight percentage Fe/(Fe + Ce) of about 2.9%, compatible with the maximum percentage of iron inside the ceria structure of about 2.5% estimated taking into account the weight percentage of hematite from Rietveld analysis.

N_2 physisorption isotherms are reported in Figure 7 and BET specific surface area of CeO_2 and Fe doped-CeO_2 catalysts are summarized in Table 2. All isotherms can be classified as type IIb, with the presence of a hysteresis loop, typical of non-porous

Research Article
doi.org/10.1002/cplu.202400521
Chemistry Europe
European Chemical Societies Publishing

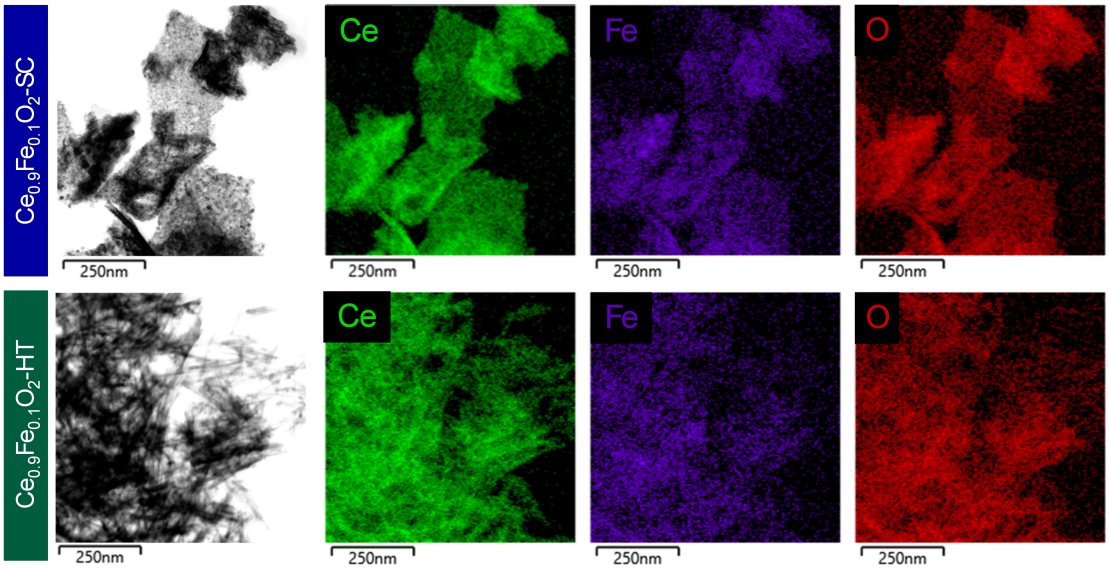

Figure 6. STEM-EDX analysis in high resolution TEM for the Fe-doped CeO_2 synthetized by SC and HT methods.

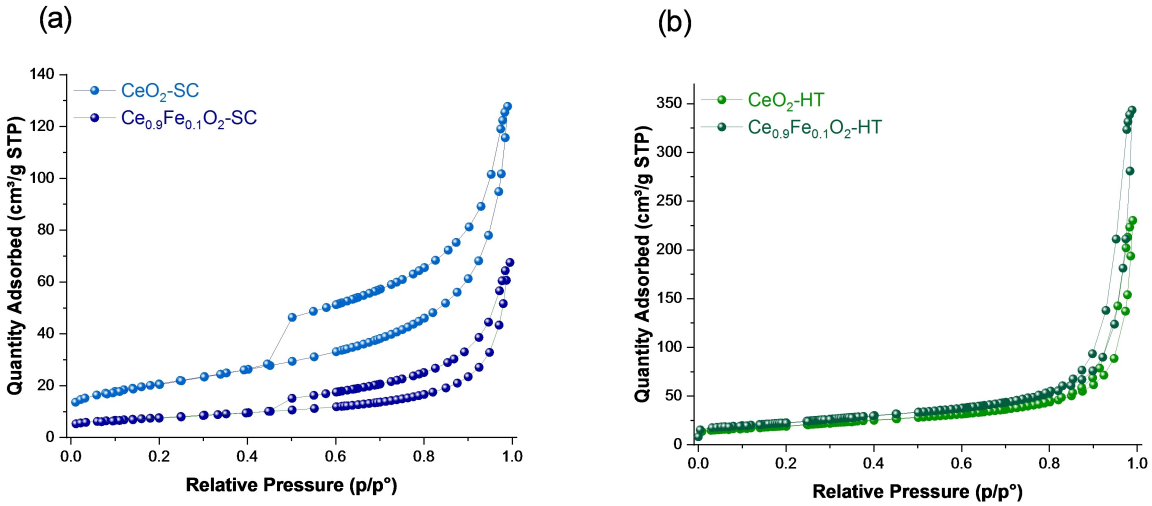

Figure 7. N_2 physisorption isotherms of CeO_2 and Fe-doped CeO_2 synthesized by SC (a) and HT (b) methods.

or macroporous solids. However, in the case of SC samples the typical trend of materials made up of platelet particles that lead to intraparticle mesoporosity was observed.[69] This finding is in agreement with the TEM images previously described (Figure 4). The surface area of the CeO_2-SC of about 80 $m^2 g^{-1}$ is among the average values reported in the literature[35,36,54] for ceria prepared with different synthetic approaches but among the highest for the ceria synthesized by solution combustion, as previously cited.[54,70] Upon the iron doping, the surface area decreased to 26 $m^2 g^{-1}$, probably as a consequence of the increase in the crystallite size. For the HT samples, the narrow hysteresis cycle is the result of the interparticle capillary condensation in the non-rigid aggregates.[69] The shape of the physisorption isotherms as well as the values of surface area, pore volume and mean pore size are in agreement with those reported in the literature for ceria nanorods prepared by hydrothermal synthesis.[36,38]

Based on the data reported in the literature, preliminary tests were performed at 140 °C under different experimental conditions in terms of amount of catalyst (from 0.1 g to 0.3 g), CO_2 pressure (from 3.0 MPa to 5.0 MPa), methanol volume (from 15 mL to 35 mL), reaction time (from 2 h to 6 h). DMC was identified as the only product in all the performed tests. Pure CeO_2 catalysts prepared by HT and SC can catalyze the direct synthesis of dimethyl carbonate, with different extent depending on the catalytic conditions. For this explorative study, CeO_2-HT was used as benchmark reference and for the set-up of the experimental apparatus, considering the promising performances derived from its elongated shape and the richness of the literature on this system.[36,38]

The results of DMC yield with the prepared CeO_2-HT sample spanned from 0.7 $mmol_{DMC} g_{cat}^{-1}$ to 3.8 $mmol_{DMC} g_{cat}^{-1}$, depending on the experimental conditions used (Table S3 and Figure 8). These values are in the range of the yields reported in

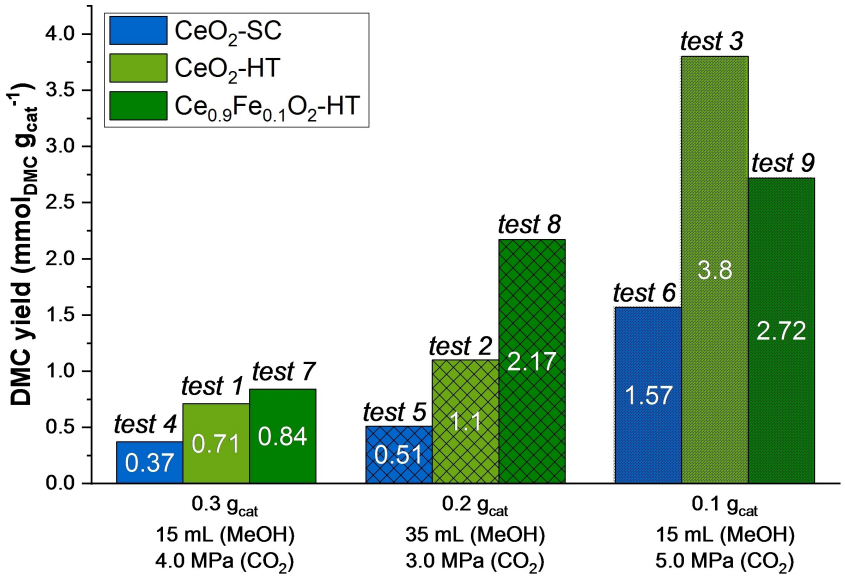

Figure 8. DMC yield values under different experimental conditions.

the literature for this type of catalyst, which range from 0.2 $mmol_{DMC}\,g_{cat}^{-1}$ to about 15 $mmol_{DMC}\,g_{cat}^{-1}$.[38,39] The wide range of DMC yields, obtained in different experimental conditions, hampers a straightforward interpretation of the results. Indeed, some authors obtained yields of about few mmol of DMC per gram of catalyst,[31,39,71] whereas others reported values of more than one order of magnitude larger.[27,36,38,49]

The catalytic performances of ceria obtained by SC method under different experimental conditions have been compared with those of the internal benchmark (CeO_2-HT) and the results are summarized in Table 3 and Figure 8.

The catalytic activity of CeO_2-SC was about half of the activity of CeO_2-HT, at the same reaction conditions. Nevertheless, an improvement of the DMC yield from 0.37(3) to 0.51(1) $mmol_{DMC}\,g_{cat}^{-1}$ was found, changing the conditions from test 4 to test 5 (Table 3 and Figure 8), similarly to what obtained for CeO_2-HT although to a different extent (+38% for CeO_2-SC and +55% for CeO_2-HT). A further increase in the catalytic activity of CeO_2-SC was revealed during test 6, when the CO_2 pressure was set at 5.0 MPa, whereas the methanol volume and catalyst amount were lowered (the mol_{MeOH}/g_{cat} ratio being similar to that of test 5). Under these conditions, a value of 1.57 $mmol_{DMC}\,g_{cat}^{-1}$ (Table 3 and Figure 8, test 6) was reached, which is about 3 folds the yield of DMC obtained at 3.0 MPa (test 5). A similar behavior was observed for the CeO_2- HT catalyst, for which the DMC yield increased from 1.1 $mmol_{DMC}\,g_{cat}^{-1}$ to 3.8 $mmol_{DMC}\,g_{cat}^{-1}$(Table 3 and Figure 8, test 2 and test 3). These results indicate that the pressure has a significant effect on the DMC yield, probably because of the amount of CO_2 solubilized in the liquid phase. As a general trend, the activity of CeO_2-HT was higher than that of CeO_2-SC at the same reaction conditions. These results are in agreement with the higher concentration of oxygen vacancies (O_v) and consequently, higher Ce^{3+} (g = 1.96) on the CeO_2-HT surface, as shown in the EPR spectrum (Figure 9), which presents a large signal at g = 2.74 related to ferromagnetic ordering. In fact, it has been widely shown in the literature that the activity of CeO_2-based materials toward DMC production is correlated with the concentration of oxygen vacancies.[34,36,37,72]

Table 4 lists the results obtained for the Fe-doped CeO_2 samples obtained by the two synthesis methods (SC and HT). It can be noted that $Ce_{0.9}Fe_{0.1}O_2$ – SC shows a negligible catalytic activity regardless of the adopted experimental conditions

Table 3. Experimental conditions adopted during the catalytic tests at T = 140 °C and corresponding values of the DMC yield for CeO_2-HT and CeO_2-SC.

Catalyst	Test #	Amount of catalyst (g)	MeOH (mL)	mol MeOH/g cat	Pressure (MPa)	Reaction time (h)	DMC yield ($mmol_{DMC}\,g_{cat}^{-1}$)
CeO_2 – HT	1	0.3	15	1.2	4.0	3	0.71
CeO_2 – HT	2	0.2	35	4.4	3.0	2	1.1(1)[a]
CeO_2 – HT	3	0.1	15	3.7	5.0	3	3.8(3)
CeO_2 – SC	4	0.3	15	1.2	4.0	3	0.37(3)
CeO_2 – SC	5	0.2	35	4.4	3.0	2	0.51(1)
CeO_2 – SC	6	0.1	15	3.7	5.0	3	1.57

[a] Average value obtained from 3 tests carried out in two different laboratories.

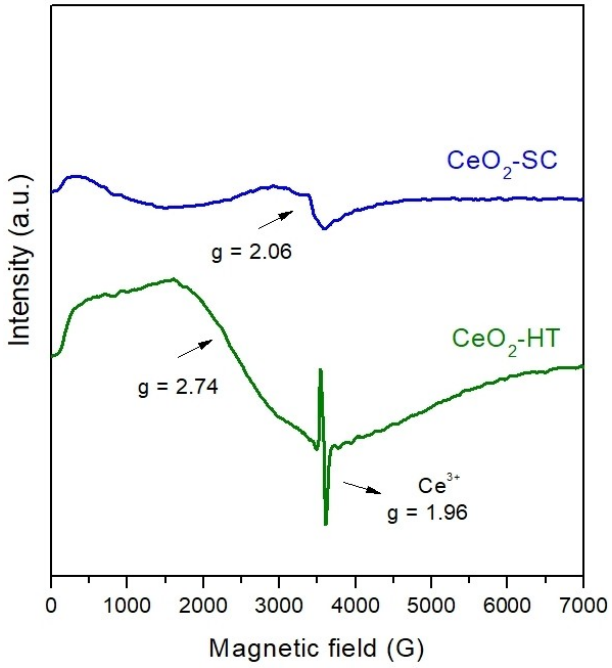

Figure 9. EPR spectra of CeO_2-SC and CeO_2-HT.

(tests 10 and 11). In the case of $Ce_{0.9}Fe_{0.1}O_2-HT$ an improvement of DMC yield from 2.17 $mmol_{DMC}\,g_{cat}^{-1}$ to 2.72 $mmol_{DMC}\,g_{cat}^{-1}$ can be observed when the CO_2 pressure is increased from 3.0 MPa to 5.0 MPa (tests 8 and 9), although to a lower extent than those observed for both the pure HT and SC CeO_2 samples. In agreement with what observed in the present case, Luo and co-workers observed an improvement of the catalytic activity for Fe-doped rod-shaped catalysts, and a worsening for nanocubes and nanoparticles with irregular shape.[39] In particular, DMC yields from 0.2 $mmol_{DMC}\,g_{cat}^{-1}$ for the pure ceria to 2.6 $mmol_{DMC}\,g_{cat}^{-1}$ for the system with 2% of iron were reported for nanorods at 3.0 MPa, 160 °C, and 4 h of reaction. Noteworthy, in similar reaction conditions, we obtained a DMC yield 6 times higher (3.8 $mmol_{DMC}\,g_{cat}^{-1}$) for CeO_2 -HT and a value comparable to that of Luo and co-workers for $Ce_{0.9}Fe_{0.1}O_2-HT$ (2.72 $mmol_{DMC}\,g_{cat}^{-1}$).

Since the iron-containing CeO_2 catalysts present ferromagnetic properties, EPR measurements are not suitable for the assessment of the oxygen vacancies, which, as already mentioned, are responsible for the different catalytic activity of the pure CeO_2 materials. Nevertheless, by considering that basic sites are important for the adsorption of CO_2 and methanol, which subsequently leads to the formation of the methoxy carbonate anion,[73] the catalysts were investigated by CO_2-TPD. By taking into account that acid sites are also reported to affect the catalytic activity,[38,39,74] the acidic properties were assessed by NH_3-TPD. The TPD profiles are shown in Figures S10 and S11 and the results are summarized in Figure 10 and Table S4 for basicity and acidity, respectively. In both cases, the desorption peaks located below 200 °C, in the range 200–400 °C, and above

Table 4. Experimental conditions adopted during the catalytic tests at T = 140 °C and corresponding values of the DMC yield for $Ce_{0.9}Fe_{0.1}O_2$-HT and $Ce_{0.9}Fe_{0.1}O_2$-SC.

Catalyst	Test #	Amount of catalyst (g)	MeOH (mL)	mol MeOH/g cat	Pressure (MPa)	Reaction time (h)	DMC yield ($mmol_{DMC}$ $gcat^{-1}$)
$Ce_{0.9}Fe_{0.1}O_2-HT$	7	0.3	15	1.2	4.0	3	0.84
$Ce_{0.9}Fe_{0.1}O_2-HT$	8	0.2	35	4.4	3.0	2	2.17(3)
$Ce_{0.9}Fe_{0.1}O_2-HT$	9	0.1	15	3.7	5.0	3	2.72
$Ce_{0.9}Fe_{0.1}O_2-SC$	10	0.2	35	4.4	3.0	2	0.05
$Ce_{0.9}Fe_{0.1}O_2-SC$	11	0.1	15	3.7	5.0	3	< LOD

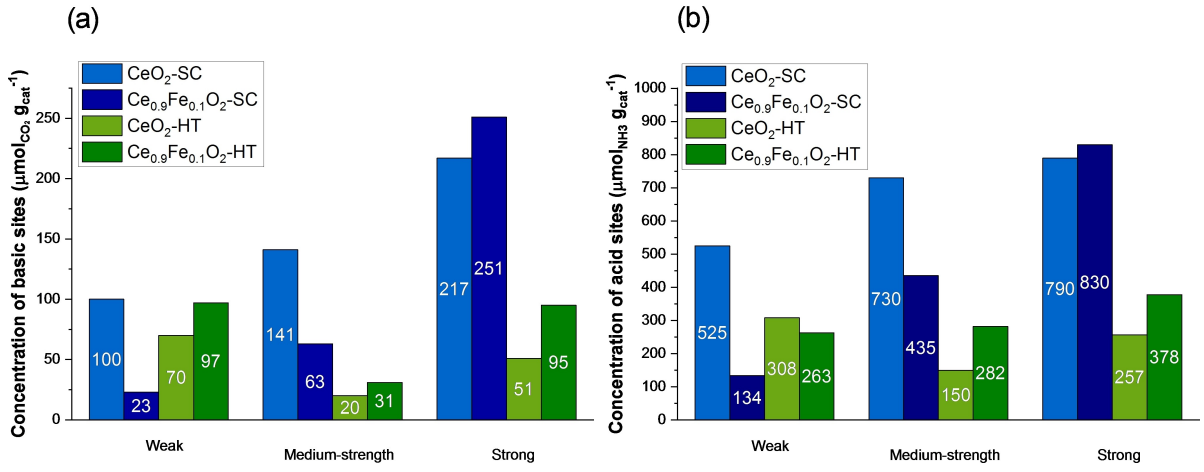

Figure 10. Concentration of basic (a) and acid sites (b) of different strength for CeO_2 and Fe-doped CeO_2 synthesized by SC and HT methods.

400 °C are attributed to weak, medium-strength, and strong sites, respectively.

The CeO_2-SC sample shows the highest concentration of both basic and acid sites (Figure 10 and Table S4), the strong ones accounting for 47% and 39% of the total sites, respectively. The obtained values are comparable with those reported in a previous work for CeO_2 nanospindles, for which the number of total acid sites was found to be more than three-fold higher in comparison with that of the total basic ones.[42]

Besides the low number of oxygen vacancies, the moderate catalytic performance of the CeO_2-SC sample could also be interpreted on the basis of the high concentration of strong basic sites, on which CO_2 is irreversibly adsorbed and, therefore, not available for DMC formation at the investigated temperature (140 °C). In addition, the presence of a high percentage of strong acid sites could also depress the catalytic activity, as reported in the literature.[71,74]

For both basic and acid sites, iron doping of the CeO_2-SC sample led to a remarkable decrease in the concentration of weak and medium-strength sites, and to an increase in that of the strong ones. In addition, the $Ce_{0.9}Fe_{0.1}O_2-SC$ catalyst presented the lowest surface area among the tested catalysts, which might also contribute to its poor activity.

On the contrary, compared to CeO_2-HT, the $Ce_{0.9}Fe_{0.1}O_2$-HT sample shows a general increase in all types of basic and acid sites, in agreement with what observed by Luo for similar samples.[39] The increase in the concentration of the weak and medium-strength sites might justify the improvement of the DMC yield for two catalytic conditions (test 7 *vs.* test 1 and test 8 *vs.* test 2). However, these favorable conditions no more hold when an increased amount of solubilized CO_2 (at higher CO_2 pressure) is present together with a lower amount of catalyst; in this case more CO_2 molecules would adsorb on the strong basic sites partially suppressing DMC formation. This finding confirms that the increase in the concentration of strong sites plays a crucial role in determining the catalytic activity.

On the basis of the obtained catalytic data together with the characterization (EPR and CO_2/NH_3-TPD measurements) we can confirm that the most common accepted mechanism proposed in the literature[38,39,47] can be applied also in our systems for the direct synthesis of DMC, as described in Figure S12.

Conclusions

In this work, the solution combustion (SC) approach was selected for the synthesis of crystalline nanoparticles of ceria to be employed for the direct synthesis of dimethyl carbonate from CO_2, due to the possibility to produce highly voluminous nanopowders ready for use without further post-synthesis treatment (*i.e.*, separation, washing and calcination) within very short times (2–3 hours), by low costs of synthesis in terms of both equipment and reactants and producing non-toxic gaseous species (eco-friendliness). Anisometric platelet ceria-based nanoparticles were obtained by using glycine or citric acid as complexing/reducing agent, and with the latter, having higher surface area and smaller crystallite size. For comparison purposes, CeO_2 nanorods prepared by hydrothermal (HT) method with a synthesis time of about 4 days was synthesized. Furthermore, the effect of the iron incorporation for both systems (SC and HT) on the microstructural, morphological, textural properties and performances was investigated, since the substitution of cerium with other metals is a suggested strategy to tailor the catalytic performances by acting on the defectivity of the system. More specifically, anisometric platelike CeO_2 nanoparticles were obtained by the SC method and tested for the first time for the direct synthesis of DMC from CO_2 due to their potential to expose the most active crystal planes. In addition, the adoption of the SC method allowed the obtainment of homogenous Fe-doped ceria, whereas a small percentage (2%wt.) of hematite was found together with the Fe-doped ceria from hydrothermal method, although the same ratio between the cerium and iron precursors was used for the syntheses. An increase (from ≈6 nm to ≈17 nm) or a decrease (from ≈21 nm to ≈16 nm) in the crystallite size of cubic ceria was found for SC and HT Fe-doped samples, respectively, in comparison with their undoped ceria counterparts. The catalytic activity of the samples prepared by HT was significantly higher than that of the samples prepared by SC. This finding can be explained mainly by the lower concentration of oxygen vacancies in the SC samples probably due to the lower exposure of the most defective active planes (111 and 110). Another key factor that influences the catalytic performance is the concentration of strong acid and basic sites, where most of the CO_2 molecules are irreversibly adsorbed on the latter at the reaction temperature of 140 °C, not being available to form DMC and poisoning the catalyst surface. The higher concentration of these sites justify the lower values of DMC yield for SC samples. Finally, the effect of the Fe-doping on the catalytic performances differed for the two systems. For the $Ce_{0.9}Fe_{0.1}O_2$-SC sample, the reaction is considerably suppressed due to a low surface area and a high concentration of strong basic sites together with a low amount of weak and medium-strength ones. For $Ce_{0.9}Fe_{0.1}O_2$-HT an improvement of the DMC yield is obtained under specific experimental conditions, most probably due to the increase in the absolute amount of active basic sites (weak and of medium strength) with respect to the CeO_2-HT. Moreover, the catalytic activity was found to strongly change depending on the experimental conditions by making more important the role of specific basic sites (strong rather than weak and of medium strength).

Supporting Information Summary

The authors have cited additional references within the Supporting Information.[75–78] The Supporting Information includes Figure S1 Pressurized reactors used to conduct the direct synthesis of DMC from CO_2; Figure S2 XRD patterns (a) and N_2 physisorption isotherms (b) of CeO_2 SC sample synthesized by citric acid and glycine as complexing agents; Figure S3 Rietveld analysis of the XRD pattern of CeO_2-GLY (a) and CeO_2-SC (b); Figure S4 Rietveld analysis of the XRD pattern of $Ce_{0.9}Fe_{0.1}O_2$

-SC; Figure S5 Rietveld analysis of the XRD pattern of CeO_2-HT; Figure S6 Rietveld analysis of the XRD pattern of $Ce_{0.9}Fe_{0.1}O_2$-HT; Figure S7 STEM-EDX analysis in conventional TEM for the Fe-doped CeO_2 synthetized by SC and HT methods; Figure S8 Wide area EDX microanalysis in high resolution TEM for the samples $Ce_{0.9}Fe_{0.1}O_2$ -SC; Figure S9 Wide area EDX microanalysis in high resolution TEM for the samples $Ce_{0.9}Fe_{0.1}O_2$ -HT; Figure S10 CO_2 -TPD profiles for the SC (a) and HT (b) samples; Figure S11 NH_3 -TPD profiles for the SC (a) and HT (b) samples; Figure S12 Schematic representation of the possible mechanism of DMC synthesis; Table S1 Synthetic methodologies used for producing Ce based catalyst for direct synthesis of DMC; Table S2 Ionic radius for different chemical species of Ce and Fe. LS: low spin state; HS: high spin state; Table S3 Experimental conditions adopted during the catalytic tests with the corresponding values of the methanol conversion and the DMC yield for ceria nanorods synthesized by hydrothermal method in this work and reference studies from the literature; Table S4 Basicity and Acidity of the SC and HT samples.

Acknowledgements

Alkeemia S.p.A. is acknowledged for financing the Ph.D. grant and the research project of Nicoletta Rusta. We are grateful for the support of Prof. Delia Gazzoli for the analysis and interpretation of Raman Spectroscopy data. Thanks are due to Dr. Andrea Ardu and to the "Centro Servizi di Ateneo per la Ricerca (CeSAR)" for the use of the TEM measurements performed with JEOL JEM 1400 PLUS and also the Multiuser Laboratory of Nanoscience and Nanotechnology (LABNANO) from the Brazilian Center of research in Physics (CBPF). The financial support of European Union NextGenerationEU under the National Recovery and Resilience Plan (NRRP) of Ministero dell' Università e della Ricerca (MUR), Project Code PE0000021, Network 4 Energy Sustainable Transition, NEST, is acknowledged. Open Access publishing facilitated by Università degli Studi di Cagliari, as part of the Wiley - CRUI-CARE agreement.

Conflict of Interests

The authors declare no conflict of interest.

Data Availability Statement

The data that support the findings of this study are available on request from the corresponding author. The data are not publicly available due to privacy or ethical restrictions.

Keywords: Ceria nanoparticles · CO_2 chemical conversion · Dimethyl carbonate · Heterogeneous catalysis · Solution combustion

[1] S. Mohammed, F. Eljack, S. Al-Sobhi, M.-K. Kazi, *J. Clean. Prod.* **2024**, *447*, 141506.
[2] D. Baskaran, P. Saravanan, L. Nagarajan, H.-S. Byun, *Chem. Eng. J.* **2024**, *491*, 151998.
[3] H. Mikulčić, I. Ridjan Skov, D. F. Dominković, S. R. Wan Alwi, Z. A. Manan, R. Tan, N. Duić, S. N. Hidayah Mohamad, X. Wang, *Renew. Sustain. Energy Rev.* **2019**, *114*, 109338.
[4] L. Fu, Z. Ren, W. Si, Q. Ma, W. Huang, K. Liao, Z. Huang, Y. Wang, J. Li, P. Xu, *J. CO2 Util.* **2022**, *66*, 102260.
[5] R. Ye, L. Ma, J. Mao, X. Wang, X. Hong, A. Gallo, Y. Ma, W. Luo, B. Wang, R. Zhang, M. S. Duyar, Z. Jiang, J. Liu, *Nat. Commun.* **2024**, *15*, 2159.
[6] L. Atzori, S. Lai, M. G. Cutrufello, F. Ferrara, A. Pettinau, M. Mureddu, E. Rombi, *J. Porous Mater.* **2024**, *31*, 281–294.
[7] G. Centi, S. Perathoner, *Catal. Today* **2009**, *148*, 191–205.
[8] C. Wei, H. Ding, Z. Zhang, F. Lin, Y. Xu, W. Pan, *Int. J. Hydrogen Energy* **2024**, *58*, 872–891.
[9] E. Catizzone, G. Bonura, M. Migliori, F. Frusteri, G. Giordano, *Molecules* **2017**, *23*, 31.
[10] F. Secci, M. Sanna Angotzi, V. Mameli, S. Lai, P. A. Russo, N. Pinna, M. Mureddu, E. Rombi, C. Cannas, *Catalysts* **2023**, *13*, 505.
[11] P. Kumar, L. Matoh, R. Kaur, U. L. Štangar, *Fuel* **2021**, *285*, 119083.
[12] Y. G. Lee, H. U. Lee, J. M. Lee, N. Y. Kim, D. H. Jeong, *Korean J. Chem. Eng.* **2024**, *41*, 117–133.
[13] P. Tundo, M. Selva, *Acc. Chem. Res.* **2002**, *35*, 706–716.
[14] S. Liu, D. Zhang, Y. Wang, F. Yang, J. Zhao, Y. Du, Z. Tian, C. Long, *Foods* **2022**, *11*, 2328.
[15] M. Zhang, Y. Xu, B. L. Williams, M. Xiao, S. Wang, D. Han, L. Sun, Y. Meng, *J. Clean. Prod.* **2021**, *279*, 123344.
[16] W. Zhu, X. Huang, C. Li, Y. Xiao, D. Zhang, G. Guan, *Polym. Int.* **2011**, *60*, 1060–1067.
[17] N. Keller, G. Rebmann, V. Keller, *J. Mol. Catal. A Chem.* **2010**, *317*, 1–18.
[18] M. Amine, Y. Barakat, *Sci. Rep.* **2023**, *13*, 14551.
[19] P. T. Coman, S. Mátéfi-Tempfli, C. T. Veje, R. E. White, *J. Electrochem. Soc.* **2017**, *164*, A1858–A1865.
[20] W. Peng, N. Zhao, F. Xiao, W. Wei, Y. Sun, *Pure Appl. Chem.* **2011**, *84*, 603–620.
[21] Y. Xiao, B. Lei, H. Jiang, Y. Xie, J. Du, W. Xu, D. Ma, M. Zhong, *J. Environ. Sci.* **2024**, DOI: 10.1016/j.jes.2024.05.048.
[22] Y. Cao, H. Cheng, L. Ma, F. Liu, Z. Liu, *Catal. Surv. from Asia* **2012**, *16*, 138–147.
[23] W. Y. Hong, *Carbon Capture Sci. Technol.* **2022**, *3*, 100044.
[24] F. Wang, T. Wan, Y. Xue, L. Cui, B. Da, N. Liu, Q. Ma, J. Xu, B. Xue, *React. Kinet. Mech. Catal.* **2023**, *136*, 2941–2954.
[25] T. Zhao, X. Hu, D. Wu, R. Li, G. Yang, Y. Wu, *ChemSusChem* **2017**, *10*, 2046–2052.
[26] Q. Yang, H. Wang, X. Ding, X. Yang, Y. Wang, *Res. Chem. Intermed.* **2015**, *41*, 4101–4111.
[27] G. Hou, Q. Wang, D. Xu, H. Fan, K. Liu, Y. Li, X. Gu, M. Ding, *Angew. Chemie Int. Ed.* **2024**, *63*, DOI: 10.1002/anie.202402053.
[28] J. Bian, M. Xiao, S. Wang, X. Wang, Y. Lu, Y. Meng, *Chem. Eng. J.* **2009**, *147*, 287–296.
[29] R. Saada, S. Kellici, T. Heil, D. Morgan, B. Saha, *Appl. Catal. B Environ.* **2015**, *168–169*, 353–362.
[30] K. Tomishige, Y. Gu, T. Chang, M. Tamura, Y. Nakagawa, *Mater. Today Sustain.* **2020**, *9*, 100035.
[31] J. Al-Darwish, M. Senter, S. Lawson, F. Rezaei, A. A. Rownaghi, *Catal. Today* **2020**, *350*, 120–126.
[32] A. H. Tamboli, N. Suzuki, C. Terashima, S. Gosavi, H. Kim, A. Fujishima, *Catalysts* **2021**, *11*, 223.
[33] U. P. S. Darbha, *J. Chem. Sci.* **2016**, *128*, 957–965.
[34] A. A. Marciniak, F. J. F. S. Henrique, A. F. F. de Lima, O. C. Alves, C. R. Moreira, L. G. Appel, C. J. A. Mota, *Mol. Catal.* **2020**, *493*, 111053.
[35] S. Wang, L. Zhao, W. Wang, Y. Zhao, G. Zhang, X. Ma, J. Gong, *Nanoscale* **2013**, *5*, 5582–5588.
[36] B. Liu, C. Li, G. Zhang, X. Yao, S. S. C. Chuang, Z. Li, *ACS Catal.* **2018**, *8*, 10446–10456.
[37] Z. Fu, Y. Zhong, Y. Yu, L. Long, M. Xiao, D. Han, S. Wang, Y. Meng, *ACS Omega* **2018**, *3*, 198–207.
[38] N. Liu, Y. Xue, Z. Yu, Y. Li, Y. Xu, J. Xu, B. Xue, J. Luo, F. Wang, *ChemistrySelect* **2023**, *8*, DOI: 10.1002/slct.202203472.
[39] M. Luo, T. Qin, Q. Liu, Z. Yang, F. Wang, H. Li, *ChemCatChem* **2022**, *14*, DOI: 10.1002/cctc.202200253.
[40] S. Wada, K. Oka, K. Watanabe, Y. Izumi, *Front. Chem.* **2013**, *1*, DOI: 10.3389/fchem.2013.00008.

[41] M. Mariyaselvakumar, T. Selvaraj, V. Balasubramanian, K. Srinivasan, *React. Kinet. Mech. Catal.* **2022**, *135*, 937–950.
[42] P. Seeharaj, T. Saenman, T. Phiwhom, C. Muangsuwan, S. Srinives, P. Kim-Lohsoontorn, *J. Environ. Chem. Eng.* **2023**, *11*, 109813.
[43] A. A. Marciniak, E. C. S. Santos, R. J. Caraballo-Vivas, O. C. Alves, M. E. H. Maia da Costa, F. Garcia, C. J. A. Mota, *Energy & Fuels* **2024**, *38*, 628–636.
[44] K. Wang, S. Li, M. Yu, X. Liang, *Energies* **2024**, *17*, 839.
[45] Y. Yoshida, Y. Arai, S. Kado, K. Kunimori, K. Tomishige, *Catal. Today* **2006**, *115*, 95–101.
[46] A. Wang, H. Wang, M. Ji, H. Yin, *New J. Chem.* **2024**, *48*, 4995–5007.
[47] B. Liu, C. Li, G. Zhang, X. Yao, S. S. C. Chuang, Z. Li, *ACS Catal.* **2018**, *8*, 10446–10456.
[48] M. Zhang, M. Xiao, S. Wang, D. Han, Y. Lu, Y. Meng, *J. Clean. Prod.* **2015**, *103*, 847–853.
[49] S. P. Wang, J. J. Zhou, S. Y. Zhao, Y. J. Zhao, X. Bin Ma, *Chinese Chem. Lett.* **2015**, *26*, 1096–1100.
[50] L. Chen, S. Wang, J. Zhou, Y. Shen, Y. Zhao, X. Ma, *RSC Adv.* **2014**, *4*, 30968–30975.
[51] N. Rusta, F. Secci, V. Mameli, C. Cannas, *Nanomaterials (Basel)* **2024**, *14*, 1490.
[52] A. Varma, A. S. Mukasyan, A. S. Rogachev, K. V. Manukyan, *Chem. Rev.* **2016**, *116*, 14493–14586.
[53] M. Zarezadeh Mehrizi, S. Ahmadi, R. Beygi, M. Asadi, *Russ. J. Non-Ferrous Met.* **2018**, *59*, 111–116.
[54] W. Kang, D. O. Ozgur, A. Varma, *ACS Appl. Nano Mater.* **2018**, *1*, 675–685.
[55] R. Bakkiyaraj, G. Bharath, K. Hasini Ramsait, A. Abdel-Wahab, E. H. Alsharaeh, S.-M. Chen, M. Balakrishnan, *RSC Adv.* **2016**, *6*, 51238–51245.
[56] T. N. Ravishankar, T. Ramakrishnappa, G. Nagaraju, H. Rajanaika, *ChemistryOpen* **2015**, *4*, 146–154.
[57] Z. Wang, J. Zhao, S. Yin, *Int. J. Appl. Ceram. Technol.* **2022**, *19*, 2990–2997.
[58] C. Cannas, A. Ardu, D. Niznansky, D. Peddis, G. Piccaluga, A. Musinu, *J. Sol-Gel Sci. Technol.* **2011**, *60*, 266–274.
[59] L. Lutterotti, P. Scardi, *J. Appl. Crystallogr.* **1990**, *23*, 246–252.
[60] R. A. Young, D. B. Wiles, *J. Appl. Crystallogr.* **1982**, *15*, 430–438.
[61] I. Kosacki, T. Suzuki, H. U. Anderson, P. Colomban, *Solid State Ion.* **2002**, *149*, 99–105.
[62] C. A. Schneider, W. S. Rasband, K. W. Eliceiri, *Nat. Methods* **2012**, *9*, 671–675.
[63] R. D. Shannon, *Acta Crystallogr. Sect. A* **1976**, *32*, 751–767.
[64] C. Schilling, A. Hofmann, C. Hess, M. V. Ganduglia-Pirovano, *J. Phys. Chem. C* **2017**, *121*, 20834–20849.
[65] A. Filtschew, K. Hofmann, C. Hess, *J. Phys. Chem. C* **2016**, *120*, 6694–6703.
[66] Y. Xu, F. Wang, X. Liu, Y. Liu, M. Luo, B. Teng, M. Fan, X. Liu, *J. Phys. Chem. C* **2019**, *123*, 18889–18894.
[67] I. H. Campbell, P. M. Fauchet, *Solid State Commun.* **1986**, *58*, 739–741.
[68] J. E. Spanier, R. D. Robinson, F. Zhang, S.-W. Chan, I. P. Herman, *Phys. Rev. B* **2001**, *64*, 245407.
[69] F. Rouquerol, *Adsorption by Powders and Porous Solids - Principles, Methodopogy and Applications.* **2014**.
[70] T. Mokkelbost, I. Kaus, T. Grande, M.-A. Einarsrud, *Chem. Mater.* **2004**, *16*, 5489–5494.
[71] S. Wang, L. Zhao, W. Wang, Y. Zhao, G. Zhang, X. Ma, J. Gong, *Nanoscale* **2013**, *5*, 5582.
[72] A. A. Marciniak, O. C. Alves, L. G. Appel, C. J. A. Mota, *J. Catal.* **2019**, *371*, 88–95.
[73] H. J. Lee, W. Joe, I. K. Song, *Korean J. Chem. Eng.* **2012**, *29*, 317–322.
[74] W. Wang, S. Wang, X. Ma, J. Gong, *Catal. Today* **2009**, *148*, 323–328.
[75] Z. Fu, Y. Yu, Z. Li, D. Han, S. Wang, M. Xiao, Y. Meng, *Catalysts* **2018**, *8*, 164.
[76] P. Kumar, P. With, V. C. Srivastava, K. Shukla, R. Gläser, I. M. Mishra, *RSC Adv.* **2016**, *6*, 110235–110246.
[77] K. H. Kang, W. Joe, C. H. Lee, M. Kim, D. B. Kim, B. Jang, I. K. Song, *J. Nanosci. Nanotechnol.* **2013**, *13*, 8116–8120.
[78] F. Siddique, S. Gonzalez-Cortes, A. Mirzaei, T. Xiao, M. A. Rafiq, X. Zhang, *Nanoscale* **2022**, *14*, 11806–11868.

Manuscript received: August 6, 2024
Revised manuscript received: September 20, 2024
Accepted manuscript online: September 20, 2024
Version of record online: ■■, ■■

RESEARCH ARTICLE

Anisometric platelet and rod-like undoped and Fe-doped ceria nanoparticles were synthesized by solution-combustion and hydrothermal method, respectively. All samples were tested as catalysts for the direct synthesis of dimethyl carbonate from CO_2 and methanol. The amount of oxygen vacancies and strong basic sites were found to be key parameters.

N. Rusta, V. Mameli, P. C. Ricci, S. Porcu, P. Seeharaj, A. A. Marciniak, E. C. S. Santos, O. C. Alves, C. J. A. Mota, E. Rombi, C. Cannas**

1 – 16

Platelet Ceria Catalysts from Solution Combustion and Effect of Iron Doping for Synthesis of Dimethyl Carbonate from CO_2